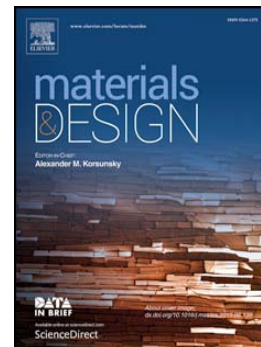# Accepted Manuscript

Perforation resistance of aluminum/polyethylene sandwich structure

Ming-ming Xu, Guang-yan Huang, Shun-shan Feng, Xiang-yu Qin, G.J. McShane, W.J. Stronge

Please cite this article as: Ming-ming Xu, Guang-yan Huang, Shun-shan Feng, Xiang-yu Qin, G.J. McShane, W.J. Stronge, Perforation resistance of aluminum/polyethylene sandwich structure, (2016), doi: 10.1016/j.matdes.2016.03.090

PERFORATION RESISTANCE OF ALUMINIUM/ POLYETHYLENE SANDWICH STRUCTURE

Ming-ming Xu[1], Guang-yan Huang[1(*)], Shun-shan Feng[1], Xiang-yu Qin[1], G.J. McShane[2(*)], W.J.Stronge[2]

[1]State Key Laboratory of Explosion Science and Technology, Beijing Institute of Technology, Beijing, P. R. China

[2]Department of Engineering, University of Cambridge, Cambridge, CB2 1PZ, UK

[(*)]*Email:* huanggy@bit.edu.cn , gjm31@cam.ac.uk

Abstract: Ballistic tests were performed on two types of polyethylene core sandwich structures (AA6082/LDPE/AA6082 and AA6082/UHMWPE/AA6082) to investigate their perforation resistance. Bulging and dishing deformation of layered plates were compared under low-velocity impact by hemispherical-nosed projectiles. Different impact failure mechanisms leading to perforation were revealed for laminates composed of a pair of aluminium alloy face sheets separated by a polyethylene interlayer. Using the finite element code Abaqus/Explicit, the perforation behaviour and distribution of energy dissipation of each layer during penetration were simulated and analysed. The deformation resistance and anti-penetration properties of polyethylene core sandwich structures were compared with those of monolithic AA6082-T6 plates that had the same areal density. Although the polyethylene interlayer enlarged the plastic deformation zone of the back face, the polyethylene core sandwich structure was a little less effective than the monolithic Al alloy target at resisting hemispherical-nosed projectile impact.

Keywords: sandwich structure, polyethylene, impact response, failure mechanisms.

1. Introduction

Sandwich structures that consist of stiff and strong face sheets bonded to a low-density core material are finding increasing use in a wide range of high-performance engineering structures, for example light-weight transport structures

designed for blast resistance [1-4]. Recent experimental studies showed that when subjected to projectile impact, sandwich structures can result in a greater dissipation of energy than monolithic plates with equal areal density [5-7]. However, Xue et al. demonstrated that a polyurea layer placed between two steel plates offered no advantage in terms of penetration resistance [8,9]. Experimental results show contradictory results for different cases. Radin et al. found that monolithic plates were better at resisting perforation due to the increased bending resistance [10]. From these investigations, we can see that the penetration resistance of sandwich structures, in comparison with alternative solutions, depends on the particular impact scenario. Whether sandwich configurations have an advantage over a monolithic plate is an open question [9].

In the current investigation, two types of polyethylene core sandwich structures (AA6082/LDPE/AA6082 and AA6082/UHMWPE/AA6082) were considered in order to investigate the influence of sandwich construction on resistance to impact deformation and penetration. The PE cores have a thickness of 6 mm, with 2 mm thick aluminium alloy face sheets in frictional contact with (not bonded to) the core. Previously, Mohagheghian et al. assessed the projectile nose shape sensitivity of impact perforation for monolithic polyethylene plates, including LDPE, HDPE and UHMWPE target panels. It was found that for blunt projectiles, and to a lesser extent round-nosed projectile, the high strain hardening of UHMWPE plays a key role in delaying localization and failure. For a conical projectile, the higher yield strength offered by high-density polyethylene (HDPE) was more important in increasing perforation resistance [11].

The present investigation first measured the static and dynamic mechanical properties of two typical semi-crystalline polyethylenes using a universal testing machine and split Hopkinson pressure bar (SPHB); the materials chosen were low-density polyethylene (LDPE) and ultra-high molecular weight polyethylene (UHMWPE). Then two types of polyethylene core sandwich structure with aluminium alloy face sheets were impacted by hemispherical-nosed projectiles across a range of impact velocities. The failure mechanisms were investigated for each layer at both low and high impact velocities. The perforation behavior and distribution of energy dissipation were calculated using the finite element code Abaqus/explicit.

2

2. Materials

This work describes the behavior of two types of polyethylene core sandwich structures under impact loading by hemispherical-nosed projectiles. The materials were non-oriented low density polyethylene (LDPE), ultrahigh molecular weight polyethylene (UHMWPE) and aluminum alloy 6082-T6. Low-density polyethylene and ultra-high molecular weight polyethylene are semi-crystalline polyethylenes, both having low density (0.91 g/cm^3 for extruded LDPE and 0.95 g/cm^3 for extruded UHMWPE) and medium strength, but with contrasting molecular weight (i.e. molecular chain length). The polyethylene material was in the form of extruded sheet. In order to build a reliable material model for impact simulations, the yield stress, ultimate strength and strain rate sensitivity are determined through quasi-static tension and compression tests and SHPB experiments. Furthermore the fracture criterion for simulation in Abaqus was based on the fracture morphology observed in ballistic impact tests. The fracture parameters for the numerical study were calibrated from the response of the monolithic LDPE and UHMWPE plates to projectiles at a range of impact velocities.

2.1. Material properties of the polymers

In the present work, quasi-static tensile and compression material tests were conducted using an INSTRON-5969 universal testing machine. The dynamic compression tests were performed on a split Hopkinson pressure bar.
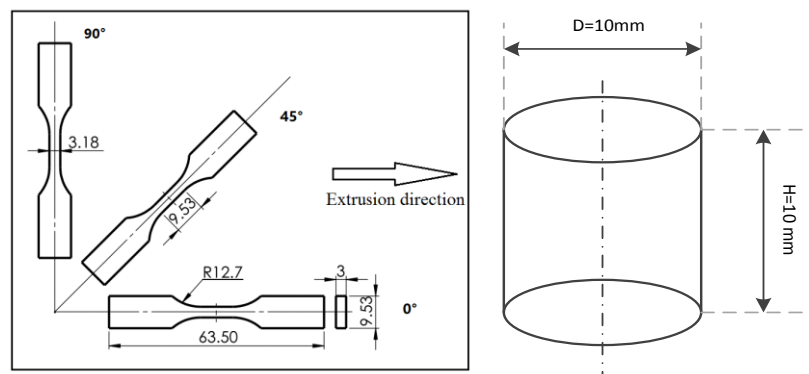

Fig. 1 Geometry of tension and compression test specimen

Specimens for tensile tests were dog-bone shaped based on the ASTM D638-03 type V specification as shown in Fig. 1. All specimens were machined from

3

extruded sheets and tested to failure. The polyethylene was tested at nominal strain rate 0.001 s^{-1} at three different orientations (0°, 45° and 90°) with respect to the extrusion direction to analyze possible material anisotropy in the plane of the extruded sheet.

A comparison of typical tensile engineering stress-strain curves for LDPE and UHMWPE at three angles (0°, 45° and 90°) and 0.001 s^{-1} strain rates are shown in Fig. 2. LDPE and UHMWPE show almost no anisotropy, as the initial slopes, representing Young's modulus E (0.87 GPa and 0.92 GPa for LDPE and UHMWPE, respectively), show little difference between the three angles. As well, the peak strengths differ by no more than 2 MPa between orientations. The mechanical properties of the extruded polyethylene sheet are therefore concluded to be approximately isotropic.
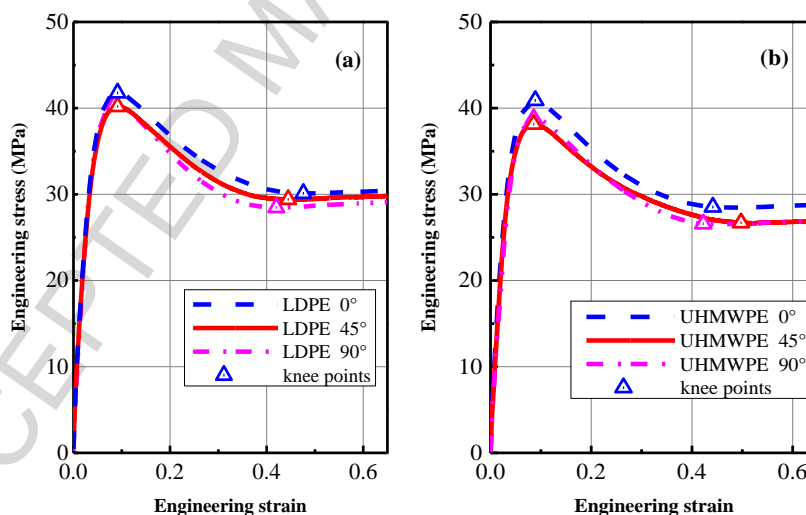
Fig. 2 Comparison of tensile engineering stress-strain curves of (a) LDPE and (b) UHMWPE in three directions at strain rate of 0.001s^{-1}

The samples for compression tests were circular cylinders 10 mm in diameter by 10 mm in length as shown in Fig. 1. In addition to quasi-static compression, dynamic testing of the LDPE and UHMWPE was performed using SHPB at strain rates from 680 s^{-1} to 3300 s^{-1} at room temperature. In Fig. 3, the compressive true stress–true strain curves for LDPE and UHMWPE are shown for six different strain rates. They present similar characteristics of yielding and plastic flow behavior, but with the UHMWPE showing more strain rate sensitivity than LDPE.

4

2.2. Modelling plasticity for polymers

Previously, a family of physically inspired constitutive equations for polymers has been established that incorporate viscoelasticity and viscoplasticity. These constitutive theories, which will be referred to subsequently as the "Arruda-Boyce" [12], "Hasan-Boyce" [13], or "Bergström-Boyce" [14,15] models, have thus far not been widely applied to semi-crystalline polymers at large deformations [16]. Hence, a non-linear constitutive model for semi-crystalline polymer materials was obtained by nonlinear fitting by Abaqus of imported quasi-static stress-strain curves for LDPE and UHMWPE measured at a strain rate 0.001 s^{-1} in compression test. Generally, a material's plastic flow stress σ_{pl} can be expressed as

$$\sigma_{pl} = f(\varepsilon_{pl}, T) \cdot \boldsymbol{R}(\dot{\varepsilon}), \tag{1}$$

where f is the quasi-static stress-strain behavior, and $\boldsymbol{R}$ is the ratio of the yield stress at any strain rate to the static yield stress.

In order to predict the yield behavior of the polyethylene specimens under a high-velocity impact, the true stress-strain curves at 0.001 s^{-1} are imported into Abaqus directly to describe the elastoplastic behavior, and a Cowper-Symonds model is used to incorporate the strain rate effect [17]. These quasi-static measurements are in agreement with those of Mohaghegian et al. [11]. The Cowper-Symonds model can be written as

$$\dot{\varepsilon}_{pl} = D(\boldsymbol{R}-1)^p, \tag{2}$$

where D and p are material parameters to be determined from experimental observations, and $\dot{\varepsilon}_{pl}$ is the strain rate. The compression experimental data at a strain rate of 0.001 s^{-1} was selected as the quasi-static value while at high strain rates; the yield stress has a power-law relationship to the static yield stress

$$\sigma_s = \sigma_0[1 + (\frac{\dot{\varepsilon}_{pl}}{D})^{1/p}]. \tag{3}$$

For both materials, the coefficients D and p of Cowper-Symonds model were identified from the yield stress measured from SHPB tests (in Fig. 3) by a regression procedure [18]. The static yield stress σ_0 is 15 MPa and 21MPa for LDPE and UHMWPE respectively, as calculated from 0.001 s^{-1} compression test.
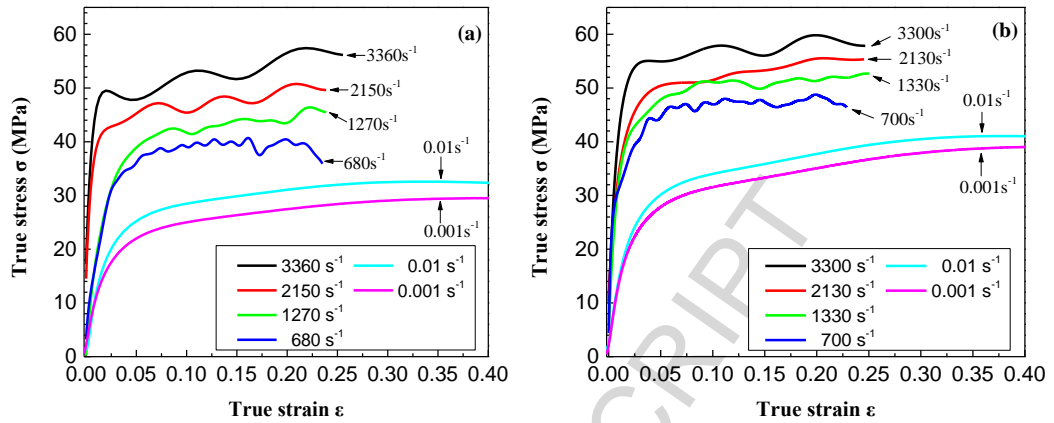
5

Fig. 3 The compression true stress-strain curves of (a) LDPE and (b) UHMWPE under a wide range of strain rates
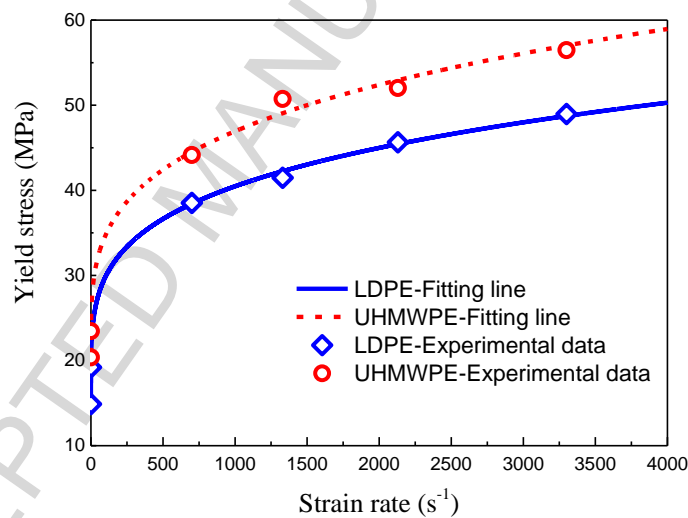

Fig. 4 The relationship between yield stress and strain rate of LDPE and UHMWPE fitted to Cowper-Symonds model

The fitting curves in Fig. 4 show the resulting Cowper–Symonds model for each material as defined by Equation (3). These curves are in good agreement with the experimental results. The non-dimensional coefficients D and p for both materials are summarized in Table 1.

Table 1 Coefficients for Cowper-Symonds model

Material	D	p
LDPE	104	4.26
UHMWPE	371	3.72

2.3. Damage criteria for polymers

According to phenomenological observations of the fracture after penetration tests, two main mechanisms can be observed in this study: ductile fracture due to

6

nucleation, growth, and coalescence of voids; and shear fracture due to shear band localization [19]. Consequently, a ductile damage criterion and shear damage criterion were applied in Abaqus. These two fracture criteria assume that the equivalent plastic strain $\bar{\varepsilon}^{pl}$ at the onset of damage is a function of stress triaxiality θ and strain rate $\dot{\bar{\varepsilon}}$. These criteria are used in combination with a damage evolution model to describe the rate of degradation of the material stiffness once the corresponding damage initiation criterion has been reached. The damage evolution law for both fracture criteria is specified in terms of equivalent plastic displacement u in linear form. Fracture of the semi-crystalline polyethylene is simulated by deleting elements once one of the failure strains for either the ductile or shear fracture criterion is satisfied. All parameters required for material damage definitions in Abaqus are listed in Table 2. The quasi-static equivalent plastic strain and displacement at failure is obtained from static tensile test results, and the parameters for dynamic behavior at high strain rate are calibrated by ballistic impact experiments.

Table 2 Parameters for fracture models and damage evolution law of polyethylene material

Materials	Ductile damage criteria				Shear damage criteria			
	$\bar{\varepsilon}_D^{pl}$	θ	$\dot{\bar{\varepsilon}}$	u	$\bar{\varepsilon}_S^{pl}$	θ	$\dot{\bar{\varepsilon}}$	u
LDPE	2.35	±0.33	0.001	0.02	2.35	1.469	0.001	0.02
	0.05	±0.33	3000	0.0007	0.05	1.469	3000	0.0007
UHMWPE	3.12	±0.33	0.001	0.04	3.12	1.469	0.001	0.04
	0.08	±0.33	3000	0.0008	0.08	1.469	3000	0.0008

2.4. Constitutive model for AA6082-T6

Aluminum alloy 6082 is a medium strength alloy with remarkable corrosion resistance. T6 implies that the alloy is heat treated and artificially aged. Aluminum alloy 6082-T6 shows excellent performance in machining operations. This grade substitutes for the conventional 6061 alloy in many structural applications where improved mechanical properties are required. It is widely used in transport and structural applications in which high strength is essential. The density of AA6082-T6 is 2.7 g/cm^3. In the present study, Aluminum alloy 6082-T6 is modeled using the Johnson–Cook constitutive model, which is widely used

for modelling impact problems [20]. In the Johnson–Cook model, the equivalent stress is expressed as the following function of the equivalent plastic strain ε_{pl}, the plastic strain rate $\dot{\varepsilon}_{pl}$, and temperature T.

$$\sigma = (A + B\varepsilon_{pl}^{n})[1 + C\ln(\dot{\varepsilon}_{pl}/\dot{\varepsilon}_0)][1 - (\frac{T - T_0}{T_{melt} - T_0})^m] \tag{4}$$

where $\dot{\varepsilon}_0$ is a reference plastic strain-rate, and A, B, n, C and m are five material constants. Constants B and n represent the strain hardening effects of the materials - these can be evaluated from the plastic portion of the stress–strain curves. T is the temperature of the material, T_0 is the reference temperature and T_{melt} is the melting temperature. In the present investigation we use a simplified form, neglecting the temperature dependence of plasticity. The other four material constants were obtained by fitting curves from the static and dynamic material tests – these are presented in Table 3. As shown in the Fig. 5, there was good agreement between the Johnson–Cook model and the experimental data measured at three strain rates. The curves show that, the AA6082-T6 is insensitive to strain rate within the range of test strain-rates that range from 0.001 s^{-1} to 0.1 s^{-1}.
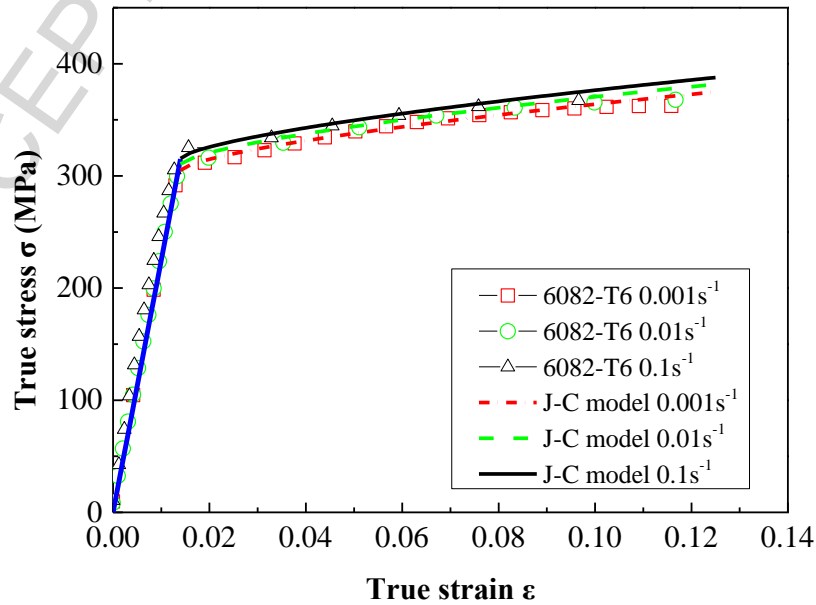

Fig. 5 Comparison of the stress–strain relations predicted by the Johnson–Cook model with compression experimental data at different strain rates

In order to calculate the fracture of aluminum sheets under impact loading, a ductile fracture model, the Johnson–Cook fracture model [21], has been used in

the finite element simulation. The Johnson–Cook fracture model that is widely used in structural reliability analyses to provide a simple mathematical relation to describe the effects of stress triaxiality, strain rate and temperature on the equivalent strain to ductile fracture

$$\varepsilon_f = [D_1 + D_2 \exp(D_3 \frac{\sigma_m}{\sigma_{eq}})][1 + D_4 \ln(\frac{\dot{\varepsilon}_{pl}}{\dot{\varepsilon}_0})][1 + D_5(\frac{T - T_0}{T_{melt} - T_0}), \qquad (5)$$

where ε_f represents the effective strain at failure, σ_m presents the hydrostatic stress, and D_1, D_2, D_3, D_4 and D_5 are five non-dimensional material constants. These constants were obtained from experiments by Ref. [22] and ballistic limits measured in this impact tests. They are listed in Table 3.

Table 3 Calibrated constants of Johnson–Cook constitutive model for AA6082-T6

Constitutive model	Parameters
Johnson–Cook model	A=305 MPa, B=304.9 MPa, C=0.0043, m=0, n=0.67
Johnson–Cook fracture model	D_1=0.059, D_2=0.246, D_3=2.41 D_4=0.05, D_5=0

3. Ballistic experiment

3.1 Experimental set-up

Experiments were conducted on a ballistic impact test system, containing four parts: ballistic gun apparatus, target, collection box and high-speed camera. The ballistic gun used in this study has a bore diameter of 13.2 mm. The inner diameter of a 13 mm standard cartridge case was refitted to 4.5 mm for improved trajectory stability. In this way, the initial velocity of the projectile can remain constant with a smaller charge. Hemispherical nosed projectiles were fired by the ballistic gun with initial velocities from 30 to 400 m/s at a normal angle of incidence to the plate. The geometric dimensions of the projectile are shown in Fig. 6. There is a tail at the rear, so the motion of the projectile, including instantaneous velocity and striking angle, can be captured during the penetration process by high speed photography and the image processing software (PCC). The projectiles were made of hardened steel with a mass of 20 g. They suffered

9

negligible plastic deformation during these experiments. Therefore, they were modelled as rigid bodies in the simulations.
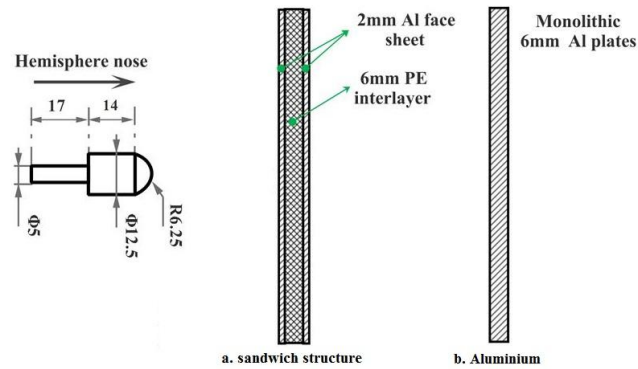

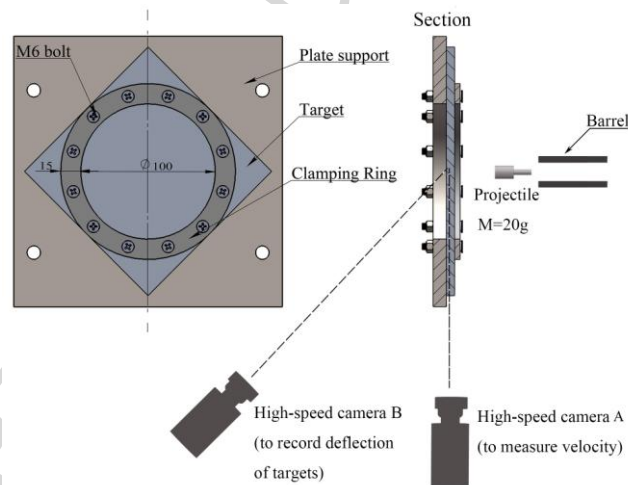**Fig. 6** Projectile geometry and target configurations

Fig. 7 Geometry of target plate fixed by steel ring on target holder

Square targets with a side length of 130 mm were selected and fixed by means of a steel ring to a thick target holder with a hole at its center. The steel ring was fastened with 12 bolts arranged on a 115 mm diameter pitch circle to provide a clamped boundary condition, as shown in Fig. 7. The targets were categorized into four groups listed in Table 4, based on the target structure and materials. A collection box was designed and put behind the targets to collect ejected fragments and projectiles during the impact test. In order to acquire a clear observation of the back surface deformation using high-speed photography, the sides of the collection box were made using impact resistant glass.

Table 4 Target plate codes

Target plate	Target material	Target thickness (mm)	Target code
Sandwich structure	LDPE	6	L6
	UHMWPE	6	U6
	AA6082-T6	2	A2
Single Al targets	AA6082-T6	6	A6

A high-speed camera system was applied using two cameras. One camera focused on the center of the target to record the ballistic trajectory, impact conditions and maximal range striking angle, while another camera at the back recorded deformation and the development of fracture in the target plates. From the digital imaging processing software PCC, important experimental data, including velocity, acceleration, flight distance and attack angle were obtained as functions of penetration time. The initial impact velocity v_i, and the residual velocity v_r, were determined by $v = \Delta d / \Delta t$, where Δd is the translation of the projectile between two frames and Δt is the recorded time interval. The frame rate was 100,000 frames per second and the resolution was 261×192 pixels for the center camera, and 20,000 frames per second and 261×192 pixels for the back camera.

Finally, the velocity results obtained from image processing were plotted and compared in $v_i - v_r$ graphs. The expression proposed by Recht and Ipson [23] was applied to fit the residual velocity curve to obtain the ballistic limits v_{bl}

$$v_r = \begin{cases} 0 & 0 \leq v_i \leq v_{bl} \\ a(v_i{}^p - v_{bl}{}^p)^{1/p} & v_i > v_{bl} \end{cases}, \tag{6}$$

where a and p are constants determined from the experimental data. Moreover constant a can be expressed as

$$a = \frac{M_p}{M_p + M_t}, \tag{7}$$

where M_p is projectile mass, and M_t is total mass of the plug punched from the plate.

11

3.2 Finite element model

Energy dissipation of each layer of sandwich structure during the penetration process is another significant factor of the penetration resistance ability of different material targets. In this paper, energy dissipation was analysed through comparison of numerical simulation results obtained from Abaqus/Explicit. As shown in Fig. 8, the circular targets plate was clamped at the edge to simulate the clamped condition in the test machine. A symmetry numerical model was used to save computation time. The targets were meshed with 8-node linear reduced integration solid 'brick' elements (C3D8R). The global element size is 1 mm with refined mesh on the plate through thickness direction (0.5 mm) and radial direction (0.8 mm). There are total 28912 elements in this model. The velocity of the rigid projectile body was controlled by reference point in a predefined field. A general penalty function contact algorithm was employed between finite elements of the projectile and plate.
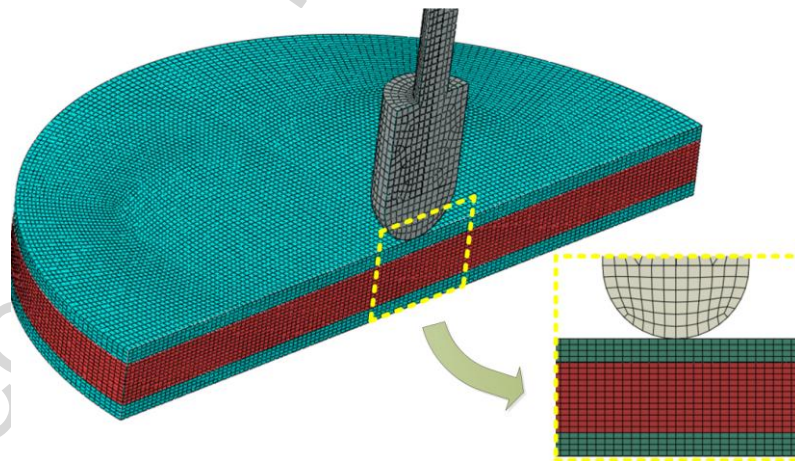

Fig. 8 Symmetry numerical model of impact test in Abaqus

4. RESULTS

4.1. Penetration and deformation process

Selections of high-speed photographs taken at 100 microsecond intervals during the penetration process for aluminum/polyethylene/aluminum sandwich plates and monolithic AA6082-T6 plates impacted by hemispherical-nosed projectiles at similar velocities are shown in Fig. 9**.** For each target, the side view is shown at the top and the back view is shown below.
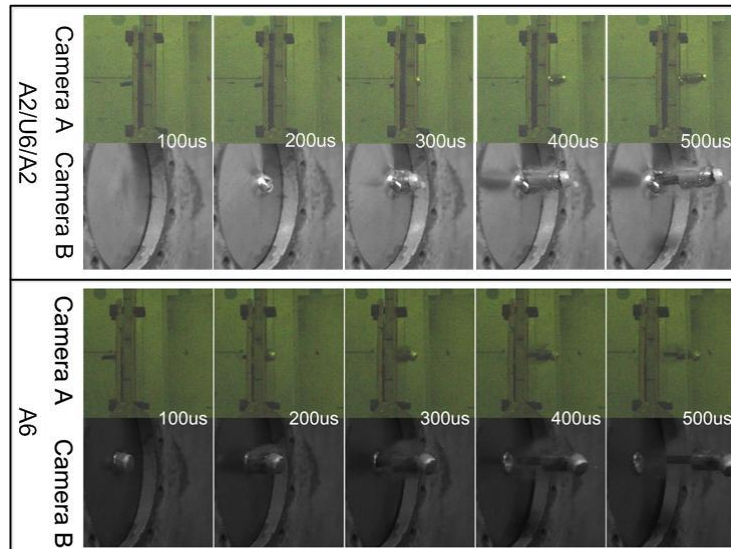
12

Fig. 9 Penetration process of A2/U6/A2 sandwich plates at 243.6m/s and monolithic AA6082-T6 plates hit at 244.2m/s

Comparing the deformation process observed from the back side of the plates, the dynamic response of the sandwich plates and monolithic AA6082-T6 plates are quite different. For polyethylene sandwich plates, the fracture of the back A2 sheet started at the center and several radial cracks propagated until the projectile and the shear plug from the front A2 plate pierce through the back plate. The back A2 sheet cracked in a petalling mode without a central plug, as observed by [24]. No large fragment of the polyethylene layer remained after perforation. For monolithic AA6082-T6 plates, the monolithic target was penetrated as a result of shear plugging around the center .The shear plug had the same diameter as the cross-section of the projectile.
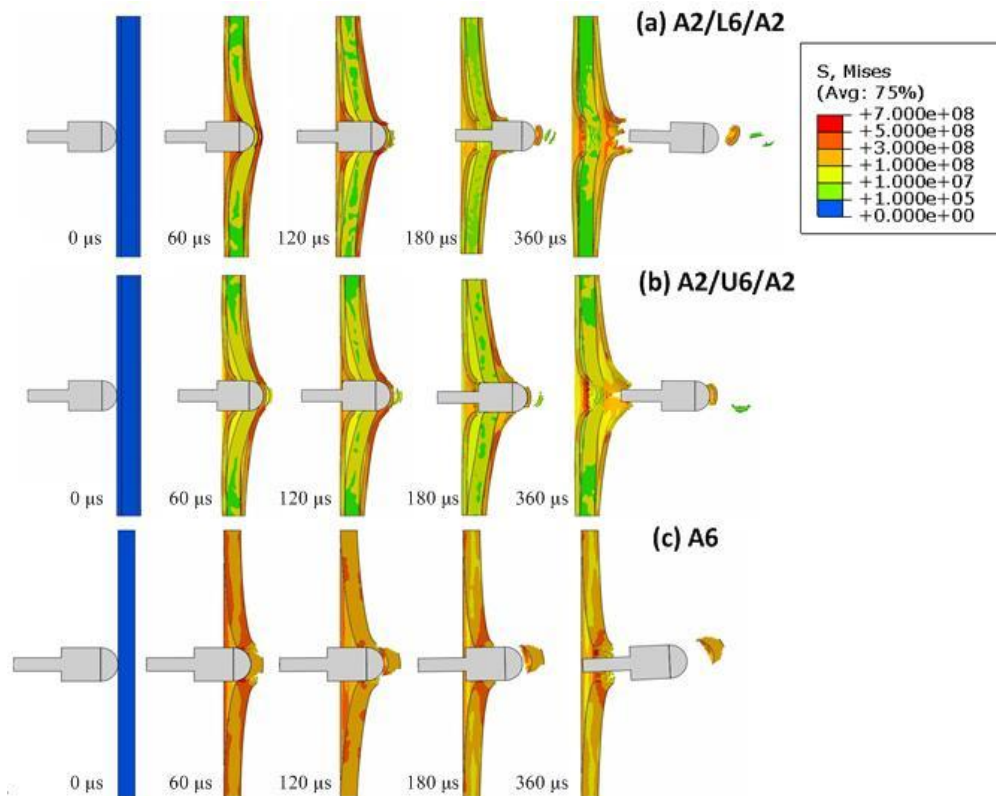
13

Fig. 10 Simulation of penetrating processes for two laminated plates (a) and (b) and one monolithic plate (c) impacted by 230m/s hemispherical nosed projectile

Simulations of the penetration process for both sandwich plates and monolithic AA6082-T6 plates impacted by a hemispherical nosed projectile are shown in Fig. 10. The two polyethylene/aluminum sandwich panels exhibited a similar deforming process. First the front A2 face sheet was penetrated by shear plugging. Next, the projectile, with the detached shear plug from the front face at its tip, pierced through the polyethylene interlayer. Subsequently the back A2 face sheet experienced global plastic bending and stretching along with the polyethylene interlayer. Finally the back A2 face sheet fractured in a petalling mode with an extensive plastically deformed zone. For monolithic AA6082-T6 plates however, the adiabatic shear plug was formed immediately and sheared from the target with highly localized plastic deformation at the projectile perimeter. It can be seen that the polyethylene interlayer diffused the concentration of the impact load, especially for the back plate, and this resulted in a larger plastically deformed zone. This will increase the total energy dissipated by the back face sheet. This perforation process will be validated in the Section on energy dissipation.
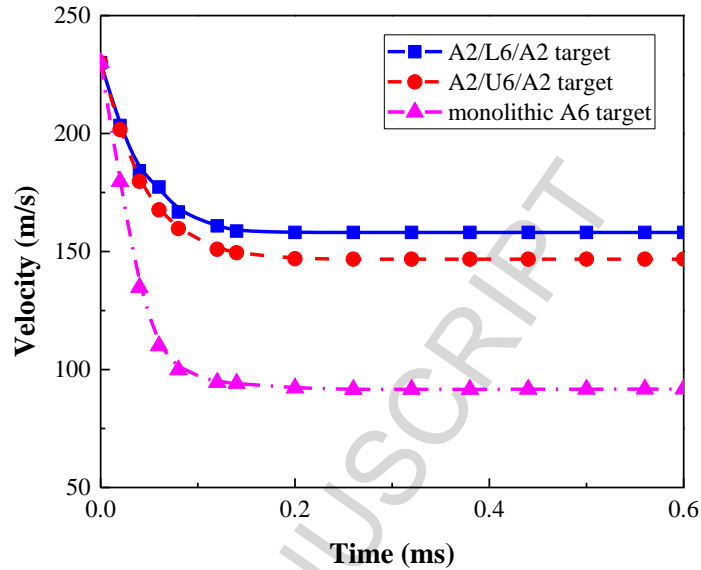
14

Fig. 11 Typical numerical simulation of *v-t* curves for penetration of three targets impacted at 230m/s by hemispherical nosed projectiles

Fig. 11 shows a detailed time-history curves for projectile velocity from finite element calculations of A2/L6/A2, A2/U6/A2 sandwich targets and monolithic A6 targets being perforated by a hemispherical nosed projectile. The velocity-time curves of L6 and U6 targets illustrate that the projectile deceleration for monolithic A6 targets was much higher than for the sandwich targets, and A2/L6/A2 sandwich targets experienced the smallest deceleration. For this hemispherical nosed projectile and a monolithic A6 target, the impact velocity of 230 m/s was close to the ballistic limit velocity. For the sandwich plates, the difference in mechanical properties between LDPE and UHMWPE interlayers made only a small difference in ballistic resistance. The calculated velocity decrease of U6 core sandwich targets was 83.2 m/s, while that of L6 core sandwich targets was 71.9 m/s. The larger velocity drop caused by the U6 interlayer is the result of the larger dynamic yield stress of UHMWPE shown in Fig. 4.

4.2. Cross section of the sandwich layers

The fracture modes and deformation of each layer of the sandwich structures are now considered, in order to analyze their capabilities for energy absorption. The cross-sections in Fig. 12 and Fig. 13 illustrate the final state of permanent deformation after impact at a low velocity and a high velocity,

15

respectly. Meanwhile, Fig. 14 reveals different failure mechanisms of the three layers in polyethylene/aluminum sandwich structures under high velocity impact.
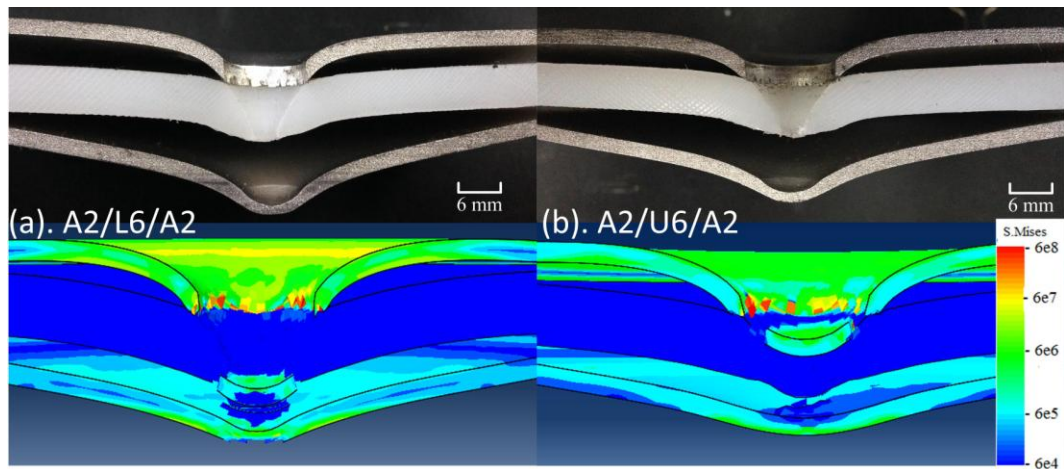

Fig. 12 Cross section of penetrated polyethylene/aluminum sandwich (a.A2/L6/A2 targets impacted by 173m/s projectile; b.A2/U6/A2 targets impacted at 176m/s)
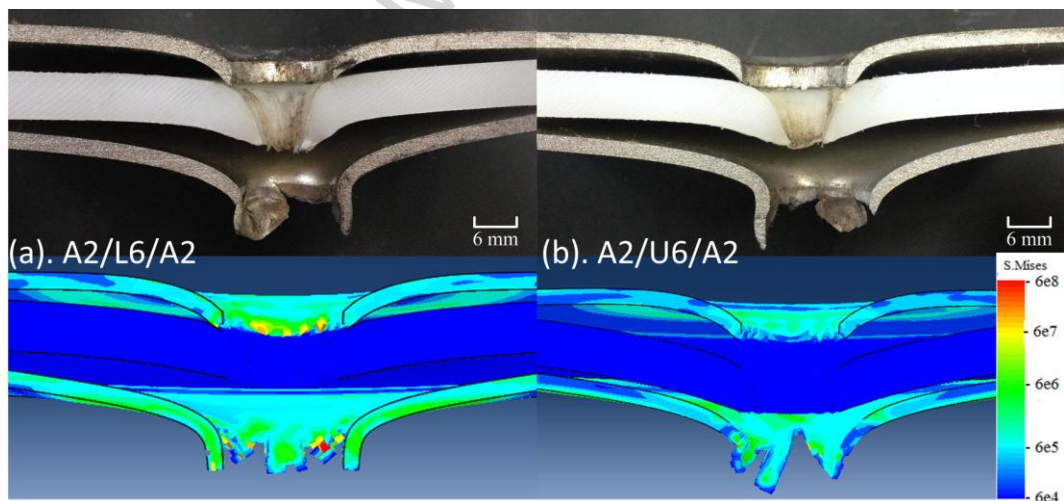

Fig. 13 Cross section of penetrated polyethylene/aluminum sandwich (a) A2/L6/A2 targets impacted by 244m/s projectile and (b) A2/U6/A2 targets impacted at 243m/s

As shown in Fig. 12 and Fig. 13, A2/L6/A2 and A2/U6/A2 sandwich panels presented similar deformation and fracture modes, as well as similar enhanced capability for plastic deformation of the back A2 sheet. For low velocity impact, the front A2 face sheet was penetrated by shear plugging with localized plastic deformation at the projectile perimeter. However, the polyethylene interlayer diffused the concentration of stress acting on the back A2 face sheet, resulting in an increased size of plastically deformed region with a hemispherical bulge at the center. The permanent deformation of the back A2 face sheet was much larger

16

than that of the front A2 face sheet. However, under high velocity impact, the central bulge on the back A2 face sheet fractured without increasing the size of the globally deformed region. Any potential enhanced performance by a polyethylene interlayer is limited due to its small elastic modulus.
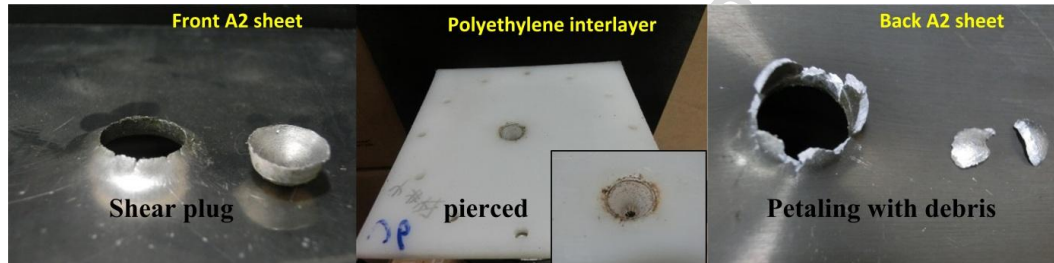

Fig. 14 Fracture face of each layer of aluminum/polyethylene/aluminum sandwich plates under high-velocity impact

The fractures developed during perforation are shown in Fig. 14. The front A2 face sheet showed a typical shear failure. The penetrating process was as follows: the polyethylene interlayer was perforated by a piercing process without forming large plugs, while the the back A2 face sheet fractured in a petaling mode with some debris. Comparing the experiments with simulated results in Fig. 12and Fig. 13, it can be seen that the simulation tests match the experiments well, which shows that the constitutive model in the simulation was practical and reliable. Though the polyethylene interlayer enlarged the plastic deformation zone of back metal sheet, it had no positive effects on the front metal sheet as there was little difference between A2/L6/A2 and A2/U6/A2 sandwich panels.

4.3. Ballistic limits

Ballistic limit velocities v_{bl} were obtained from the intersections of fitting lines for the post-perforation residual velocity and the x-axis. The experimental data are presented in **Table 5**. Fig. 15 shows a comparison of the experimental residual velocities of three panels. The constants a, p and ballistic limit determined from the simulations and experimental data are summarized in Table 6**.**

Table 5 Experimental test results of three different target panels

Targets	Test No.	v_i (m/s)	v_r (m/s)	Angle	ΔE_k(J)
A6	A#1	211.4	0	0°	446.89
	A#2	226.8	90.0	4.4°	433.38
	A#3	231.7	110.3	3.1°	415.19
	A#4	244.2	118.3	0°	456.39
	A#5	276.3	153.2	1.2°	528.71
A2/L6/A2	B#1	136.6	-17.5	2.8°	183.53
	B#2	173.0	0	2°	299.29
	B#3	204.0	61.1	5.5°	378.83
	B#4	222.1	112.4	0°	366.95
	B#5	239.7	133.6	3°	396.07
A2/U6/A2	C#1	176.6	0	6°	311.88
	C#2	197.5	54.7	2.1°	360.14
	C#3	209.2	85.4	0°	364.71
	C#4	214.5	105.6	3°	348.59
	C#5	243.6	151.6	0°	363.58
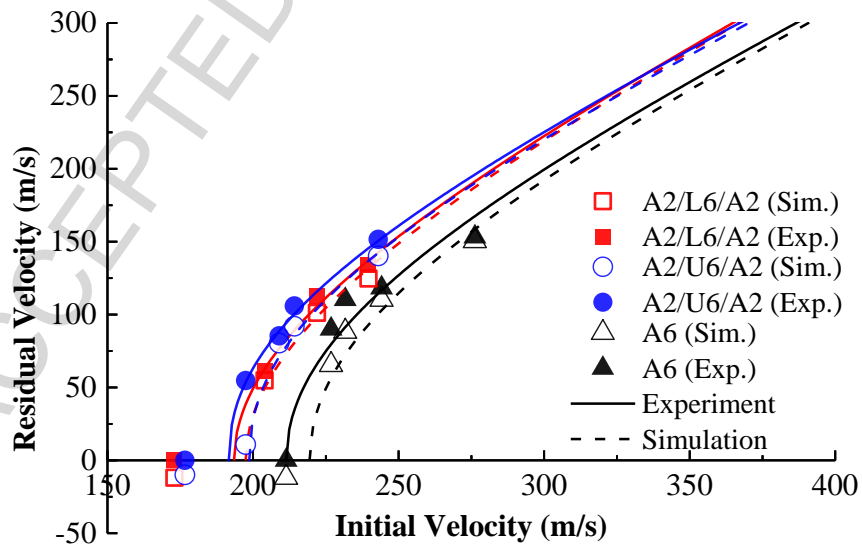
Fig. 15 Residual velocity curves for three sandwich configuration targets

The residual velocity results showed no significant difference in the measured ballistic limit velocity between the two sandwich configurations because of their similar effect on plastic deformation of the back A2 sheet. The residual velocity curves of A2/L6/A2 and A2/U6/A2 sandwich plates almost overlapped. Though the UHMWPE has higher strength than LDPE, this difference is small when compared with that of aluminum alloy, as the AA6082-T6 has an

18

order of magnitude larger yield stress than polyethylene. The perforation resistances of A2/L6/A2 and A2/U6/A2 sandwich plates are equivalent. As shown in Table 5, the kinetic energy loss of projectiles that had perforated sandwich plates was 21% less than that of monolithic A6 targets.

Table 6 Experimental and numerical ballistic limit velocities and Recht-Ipson constants

Constants	A2/L6/A2	A2/U6/A2	A6
a	0.97	0.92	0.91
p	2	2.24	2.09
Experiment v_{bl} (m/s)	193.46	191.74	211.43
Simulation v_{bl} (m/s)	197.12	198.56	219.51

In Table 6, ballistic limits obtained from numerical simulations and experiments show a good agreement. The difference between simulations and experiments is less than 8 m/s or 4%. One cause of this discrepancy is that the numerical model has neglected thermal softening and so it underestimates the residual velocity of the projectile.

4.4. Energy dissipation

As shown by previous investigation [24], during penetration of a plate impacted by a hemispherical nosed projectile at an impact velocity near the ballistic limit, approximately 80% of the loss of kinetic energy during perforation is accounted for by plastic dissipation in the target.

Fig. 16 shows the distribution of energy dissipated by plastic strain as a function of time during penetration in simulations of A2/L2/A2 and A2/U2/A2 sandwich targets and monolithic A6 targets subjected to 230 m/s impact. The energy partition among the front plate, the back plate and the polyethylene interlayer is plotted in Fig. 15(d). From Fig. 15(a) and (b), it can be seen that the energy dissipating process of A2/L2/A2 and A2/U2/A2 sandwich targets is similar. In polyethylene core sandwich targets, the back A2 face sheet dissipated 91.1 J and 101.7 J for A2/L2/A2 and A2/U2/A2 sandwich targets respectively, approximately 13 J high than the front A2 face sheet owing to its larger plastic deformation. Meanwhile the LDPE interlayer dissipated 46.9 J of energy by plastic strain, and contributed 21.3% of the total dissipated energy. In contrast, the UHMWPE interlayer dissipated 65.4 J of energy by plastic strain, and contributed

25.7% of the total dissipated energy. Compared with the energy dissipated by the monolithic A6 target (401.5 J), the energy dissipated by A2/L2/A2 and A2/U2/A2 sandwich targets are about 45% and 37% less, respectively. This is in agreement with previous experiments results.
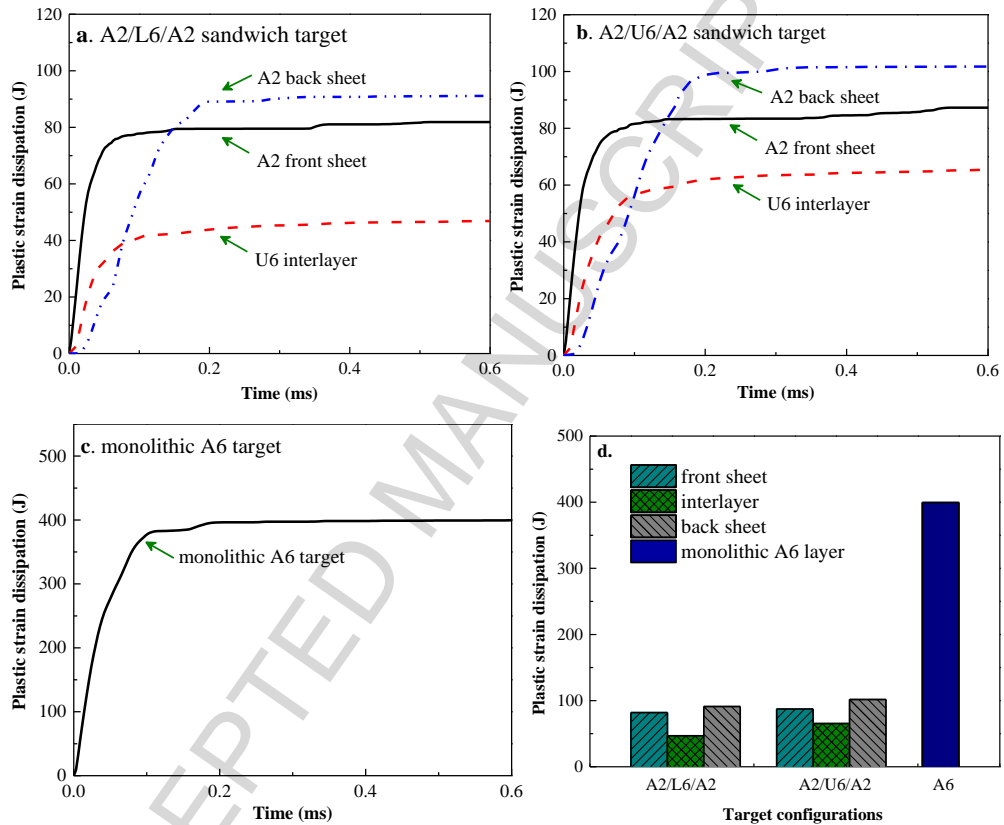

Fig. 16 Numerical prediction of energy dissipation during penetration process of three targets impacted by 526.8 J hemispherical projectiles at 230 m/s

5. Conclusions

This experimental study compared the deformation and ballistic resistance of sandwich targets and equivalent weight monolithic targets in order to develop understanding of the process of fracture development and perforation of polyethylene core sandwich panels. Numerical simulations by Abaqus/Explicit finite element code were effective and gave reference for impact damage of sandwich plates for engineering applications. A Cowper-Symonds strain rate hardening model was adopted for the polyethylene materials based on SHPB test. Fracture parameters for both the aluminum AA6082-T6 and the polyethylene materials were obtained from a subset of experiments. Based on the experimental

20

observations and numerical analyses, the following main conclusion can be drawn:

• Irrespective of the stiffness of the polymer core, perforation of laminated aluminum/polyethylene sandwich panels followed a similar process. First, the front A2 face sheet was perforated by shear plugging with localized plastic deformation at the center. Then the polyethylene interlayer diffused the concentration of impact stress, increasing the area of the back face that was subject to large pressure. Finally the back face sheet was radially cracked and then petalling occured in a global plastic deformation zone as the plug from the impact surface pushed through.

• Deformation and perforation of the proximal aluminum sheet by impact of the projectile were not affected by the stiffness of the polyethylene core.

• Comparing perforation resistance of aluminum/polyethylene/aluminum sandwich panels and monolithic aluminum sheet of equal areal density, it required 21% more energy for a hemispherical nosed projectile to perforate the monolithic aluminum plate.

• When used with high strain rate material properties obtained from SHPB and an experimentally determined equivalent plastic strain failure criterion, the finite element program Abaqus/Explicit gave calculated ballistic limit velocity within 4% of the experimentally observed ballistic limit.

Acknowledgments

References:
[1] Amini MR, Isaacs JB, Nemat-Nasser S. Experimental investigation of response of monolithic and bilayer plates to impulsive loads. INT J IMPACT ENG. 2010;37:82-9.
[2] Amini MR, Amirkhizi AV, Nemat-Nasser S. Numerical modeling of response of monolithic and bilayer plates to impulsive loads. INT J IMPACT ENG. 2010;37:90-102.
[3] Tarlochan F, Ramesh S, Harpreet S. Advanced composite sandwich structure design for energy absorption applications: Blast protection and crashworthiness. COMPOS PART B-ENG. 2012;43:2198-208.
[4] Lehmhus D, von Hehl A, Kayvantash K, Gradinger R, Becker T, Schimanski K, et al. Taking a downward turn on the weight spiral – Lightweight

materials in transport applications. MATER DESIGN. 2015;66, Part B:385-9.

[5] Zhou DW, Stronge WJ. Ballistic limit for oblique impact of thin sandwich panels and spaced plates. INT J IMPACT ENG. 2008;35:1339-54.

[6] Marom I, Bodner SR. PROJECTILE PERFORATION OF MULTI-LAYERED BEAMS. INT J MECH SCI. 1979;21:489.

[7] Dey V, Zani G, Colombo M, Di Prisco M, Mobasher B. Flexural impact response of textile-reinforced aerated concrete sandwich panels. MATER DESIGN. 2015;86:187-97.

[8] Xue L, Wierzbicki T. Numerical simulation of fracture mode transition in ductile plates. INT J SOLIDS STRUCT. 2009;46:1423-35.

[9] Xue L, Jr. Mock W, Belytschko T. Penetration of DH-36 steel plates with and without polyurea coating. MECH MATER. 2010;42:981-1003.

[10] Radin J, Goldsmith W. NORMAL PROJECTILE PENETRATION AND PERFORATION OF LAYERED TARGETS. INT J IMPACT ENG. 1988;7:229-59.

[11] Mohagheghian I, Mcshane GJ, Stronge WJ. Impact perforation of monolithic polyethylene plates: Projectile nose shape dependence. INT J IMPACT ENG. 2015;80:162-76.

[12] Boyce MC, Arruda EM, Jayachandran R. The large strain compression, tension, and simple shear of polycarbonate. Polymer Engineering & Science. 1994;34:716-25.

[13] Hasan OA, Boyce MC. A constitutive model for the nonlinear viscoelastic viscoplastic behavior of glassy polymers. Polymer Engineering & Science. 1995;35:331-44.

[14] Bergström JS, Boyce MC. Constitutive modeling of the large strain time-dependent behavior of elastomers. J MECH PHYS SOLIDS. 1998;46:931-54.

[15] Bergström JS, Boyce MC. Constitutive modeling of the time-dependent and cyclic loading of elastomers and application to soft biological tissues. MECH MATER. 2001;33:523-30.

[16] Bergström JS, Kurtz SM, Rimnac CM, Edidin AA. Constitutive modeling of ultra-high molecular weight polyethylene under large-deformation and cyclic loading conditions. BIOMATERIALS. 2002;23:2329-43.

[17] Cowper GR, Symonds PS. Strain-hardening and strain-rate effects in the impact loading of cantilever beams.: DTIC Document; 1957.

[18] Shen WQ, Jones N. Dynamic response and failure of fully clamped circular plates under impulsive loading. INT J IMPACT ENG. 1993;13:259-78.

[19] Cayzac H, Sai K, Laiarinandrasana L. Damage based constitutive relationships in semi-crystalline polymer by using multi-mechanisms model. INT J PLASTICITY. 2013;51:47-64.

[20] Johnson GR, Cook WH. A constitutive model and data for metals subjected to large strains, high strain rates and high temperatures. Proceedings of the 7th International Symposium on Ballistics: The Netherlands; 1983. p. 541-7.

[21] Johnson GR, Cook WH. Fracture characteristics of three metals subjected to various strains, strain rates, temperatures and pressures. ENG FRACT MECH. 1985;21:31-48.

[22] Zhou J, Hayden M, Gao X. An investigation of the strain rate and temperature effects on the plastic flow stress and ductile failure strain of aluminum alloys 5083-H116, 6082-T6 and a 5183 weld metal. P I MECH ENG C-J MEC. 2013;227:883-95.

[23] Ipson TW, Recht RF. Ballistic-penetration resistance and its measurement.

EXP MECH. 1975;15:249-57.

[24] Xue L, Jr. Mock W, Belytschko T. Penetration of DH-36 steel plates with and without polyurea coating. MECH MATER. 2010;42:981-1003.

Graphical abstract
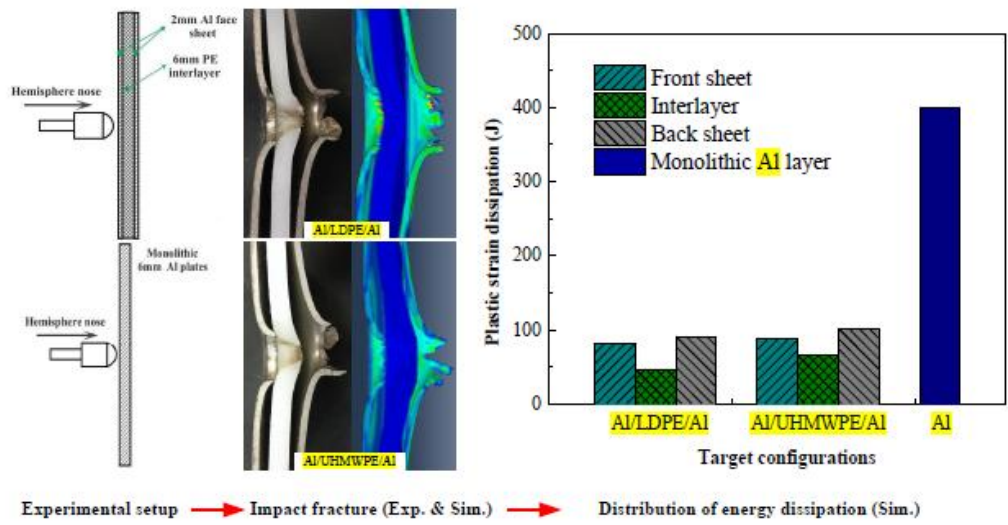
Highlights

1. Ballistic resistances of polyethylene sandwich targets were compared by experiments and simulations.

2. Ballistic limits of sandwich targets were 21% less than monolithic Al targets.

3. The polyethylene core contributed 21% of the total dissipated energy during projectile penetration.

4. 16% more energy dissipated by Al back sheet in sandwich targets than Al back sheet.